CHEMISTRY OF MATERIALS

pubs.acs.org/cm

Article

Lithium-Ion Diffusion in Near-Stoichiometric Polycrystalline and Monocrystalline $LiCoO_2$

Daniel Uxa,* Erwin Hüger, Kevin Meyer, Lars Dörrer, and Harald Schmidt

Cite This: *Chem. Mater.* 2023, 35, 3307−3315

Read Online

ACCESS | Metrics & More | Article Recommendations

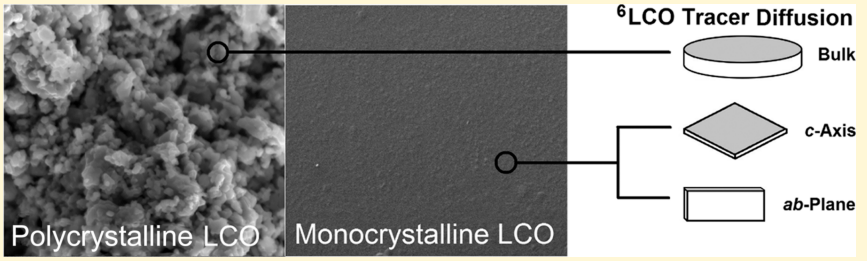

ABSTRACT: Lithium-metal-oxide-based cathode materials like $LiCoO_2$ are an essential part of lithium-ion batteries, which are intensively researched and continuously improved. For a basic understanding of kinetic processes that control lithium incorporation and removal into/from electrodes, the lithium-ion transport in the cathode material is of high relevance. This concerns lithium diffusivities, as well as defect structures, transport mechanisms, and confined diffusion paths, such as grain boundaries. In the present study, lithium tracer self-diffusion is investigated by means of isotope exchange and secondary ion mass spectrometry in polycrystalline sintered bulk samples of stoichiometric $LiCoO_2$ with an average grain size of about 70 nm and in single crystalline $LiCoO_2$ in the *ab*-plane and *c*-axis in the temperature range between 200 and 700 °C. For the polycrystals, we found an activation enthalpy of ΔH = 0.75 eV. In the single crystal, the lithium-ion diffusivities along the *ab*-plane are identical to the diffusivities in polycrystalline $LiCoO_2$. This indicates that diffusion along grain boundaries is similar to bulk diffusion and does not play a dominating role for the overall lithium-ion migration. Along the *c*-axis, diffusivities are some orders of magnitude lower, but only a slightly higher activation energy of 0.94 eV is found. This provides the experimental evidence of the often-claimed sluggish lithium diffusion along the *c*-axis. We suggest that lithium diffusion along the *c*-axis is most likely determined by fast diffusion in the *ab*-plane and a slow transfer of lithium ions across the CoO_2 layers.

1. INTRODUCTION

1.1. Lithium-Ion Batteries and $LiCoO_2$-Based Cathode Material. Lithium-ion batteries (LIBs) are rechargeable electrochemical energy storage devices based on lithium-ion insertion/extraction.[1−10] Among devices based on sodium, magnesium, and aluminum, which are increasingly studied in both academia and industry, only lithium-ion rechargeable batteries have been successfully commercialized up to now and are widely established as power sources for portable electronic devices, as well as current and future electric transport systems.[9] The LIB prototype is composed of graphite as a negative electrode (anode) and a lithium-metal-oxide as a positive electrode (cathode), separated by an electrolyte which acts as a transport medium for the lithium ions.[10] The increasing number of mobile devices with increasing demand for a higher energy density, beyond the current level, and especially the change to electromobility, with increasing demand for driving range, necessitates research to understand and improve known or find new materials (for both anodes and cathodes) for energy storage and conversion. The present cathode materials in commercial use include $LiCoO_2$ (LCO), the first and most successful form of layered transition-metal oxide cathodes, or the highly competitive but still developing LCO-derivatives $LiNi_xMn_yCo_{1-x-y}O_2$ (NMC) and $LiNi_xCo_yAl_{1-x-y}O_2$ (NCA).[3,5] $LiCoO_2$ belongs to the $LiMO_2$ (M = V, Cr, Co, Ni) series with the layered structure based on a close-packed network of oxygen atoms with the Li^+, Co^{3+}, and O^{2-} ions ordering on alternating planes. The structure crystallizes in the hexagonal α-$NaFeO_2$-type $R\bar{3}m$ space group.[11]

1.2. Lithium Intercalation/Deintercalation and Lithium-Ion Migration in $Li_{1-x}CoO_2$. As an electrode material, LCO is subjected to lithium extraction and (re-)insertion

Received: February 17, 2023
Revised: March 31, 2023
Published: April 11, 2023

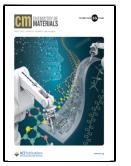

during charge and discharge, with the corresponding delithiation reaction occurring as

$$LiCoO_2 \rightarrow Li_{1-x}CoO_2 + xLi^+ + xe^-$$

The extracted lithium ions dissolve in the electrolyte, and the electrons move to the outer circuit. This process can be interpreted as the creation of electrochemically activated defects in the crystal lattice of the electrode material.[12] Due to the extraction of lithium from the solid, lithium vacancies V_{Li} are formed, where their concentration depends on the stage of lithiation/delithiation of the cathode. Oxidation occurs at the cobalt-ions, and the removal of lithium ions is compensated by the formation of hole polarons η^+ ($V_{Li} = V_{Li}^- + \eta^+$).[12] The understanding of defect physics and chemistry in complex cathode materials has improved significantly over the last decade, which gives more insight into the transport processes on the atomic scale.[12−24] The lithium-ion migration in the crystal lattice, at least for LCO with lithium deficit, is assumed to occur via the movement of negatively charged lithium vacancies in one direction, which is equivalent to that of the lithium ions in the opposite direction. It is mediated either through a monovacancy or a divacancy mechanism, with their respective calculated (DFT) migration energy barriers around 0.8 and 0.25 eV.[17,18] The divacancy mechanism is expected to be dominant in a partially delithiated LCO cathode with a high lithium vacancy concentration. In this context, an experimental investigation of lithium-ion transport (diffusivities, defect structures, diffusion mechanisms, and diffusion paths) in cathode materials such as LCO is of high relevance,[25] as it directly influences charging/discharging times (and consequently power densities), maximum capacities, stress formation (electrode stability), and possible side reactions.

1.3. On the Role of Grains, Grain Boundaries, and *c*-Axis Diffusion in $LiCoO_2$-Based Cathode Material. The perfect LCO crystal is composed of CoO_2 layers stacked in the [0001] (*c*-axis) direction, with lithium intercalated in between, which forms a 2d network parallel to the (0001) plane.[26] Due to its layered structure, LCO is expected to be a 2d lithium-ion conductor, where in-plane (*ab*-plane) diffusion is expected to be fast, but diffusion along the *c*-axis is unlikely to occur (or extremely slow) due to a very high calculated energy barrier of 6.8 eV for direct penetration through the CoO_2 layers.[26−28] Hasegawa et al.[27] discussed the possibility of *c*-axis diffusion by transfer across the CoO_2 layers via rare (low concentration) defects. Lithium antisites and oxygen vacancies with a calculated migration barrier of 1 eV are suggested. For the realization of long-range *c*-axis diffusion, the lithium ions have to move from one defect to the next via *ab*-plane diffusion.

Commercially used LCO cathode material generally consists of powder particles with polycrystalline grains. In polycrystalline LCO with grain boundaries, the displacement of CoO_2 layers leads to the creation of periodic gaps that act as diffusion channels along the *c*-axis.[26] Both Zhu et al.[26] and Moriwake et al.[28] calculated migration energy barriers for lithium-ion migration along a grain boundary in the [0001] direction and yielded 0.7 and 0.73 eV, respectively, for the monovacancy mechanism, similar to the bulk activation energy. This means that in polycrystals of LCO, the long-range lithium-ion diffusion is predicted to occur mainly via in-plane diffusion and transfer along grain boundaries within gaps in the periodic structure that act as diffusion channels.

1.4. Experimental Investigations of Lithium-Ion Diffusion in $LiCoO_2$-Based and Related Cathode Material. There are currently numerous theoretical/computational studies on lithium-ion diffusion in LCO and related cathode materials in the literature (see refs 12−24). However, the knowledge of reliable experimentally determined diffusion parameters (diffusivities, activation energies, pre-exponential factors, diffusion mechanisms) in relevant cathode materials is limited to a few experimental studies. In view of the importance of lithium-ion transport, which is often emphasized, this may come as a surprise, but it could be explained by the fact that the investigation of lithium-selective diffusion relates to a variety of analytical problems. Lithium diffusivities experimentally determined at or close to room temperature using electrochemical, application-oriented methods [electrochemical impedance spectroscopy (EIS), galvanostatic intermittent titration technique (GITT), and potentiostatic intermittent titration technique (PITT)] are in the range between 10^{-18} and 10^{-15} m^2/s for LCO.[29−31] In general, these diffusivities vary for orders of magnitude for different studies and methods and for the stage of lithiation. Electrochemical measurements of diffusivities may involve interfacial processes, ohmic resistances, and side reactions that often complicate the analysis. As recently discussed by Stolz et al.,[31] conventional galvanostatic techniques are more application-oriented than others and give kinetic insights via the characteristic overvoltage data, while the EIS technique can overemphasize certain resistance types and has an increased risk of misinterpretation.

A method that is also lithium-ion selective is nuclear magnetic resonance (NMR) spectroscopy.[32] Experimental studies with this method are limited, which is due to the strong influence of magnetism in these materials on spin relaxation processes.[32] Tomeno and Oguchi carried out a study based on NMR[33] but without specifying diffusion coefficients and activation energies. Nakamura et al.[34] performed a series of spin-relaxation investigations on LCO powder and reported very small lithium-ion migration energies of 0.076 eV above room temperature, which they attributed to interlayer migration. Similar experiments by the authors on Li_xCoO_2 powders[35] yielded 0.3 eV for $x = 1$ and $x = 0.8$ and 0.08 eV for $x = 0.6$. The difference found is attributed to two different hexagonal phases. Further investigations by Nakamura et al.[36] on lithium-ion migration in ball-milled LCO powder by complex resistivity measurements and NMR yielded activation energies between 0.29 and 0.36 eV, depending on the milling time.

Tracer methods (stable or radioactive) combined with isotope depth profiling are very well suited to study long-range and lithium-selective diffusion processes. They enable a direct measurement of the lithium tracer diffusion coefficient, without model-dependent correction factors. Lithium tracer diffusion experiments are complex because suitable radioactive tracers are not available for lithium. Therefore, the standard radiotracer technique (which is state-of-the-art for determining diffusion processes in metals and intermetallics due to its high detection sensitivity[37]) cannot be used. To circumvent this problem, stable isotopes can be used, such as ^6Li with a natural abundance of 7.5% and ^7Li with an abundance of 92.5%, where ^6Li can be used as a tracer. ^6Li-based tracer experiments using isotope heterostructures[38] and isotope depth profiling by secondary ion mass spectrometry (SIMS) were done by Uxa et al. for sintered bulk $Li_{0.9}CoO_2$[39] and

https://doi.org/10.1021/acs.chemmater.3c00359
Chem. Mater. 2023, 35, 3307−3315

$Li_{0.9}Ni_{0.33}Mn_{0.33}Co_{0.33}O_2$.[40] They found activation energies for lithium-ion migration of 0.76 and 0.85 eV, respectively. Hasegawa et al.[27] investigated lithium tracer diffusion in polycrystalline *c*-axis textured Li_xCoO_2 (x = 0.995 and 0.999) thin films by means of a "step-isotope-exchange method" and SIMS and reported an activation energy for lithium-ion migration of 0.25 eV close to room temperature. In addition, experiments on $LiNi_{0.5}Mn_{1.5}O_4$[41] and $LiMn_2O_4$[42−45] can be found in the literature.

1.5. Objective of This Study. In the present work, we investigated lithium tracer diffusion in the temperature range of 200−700 °C in near-stoichiometric sintered polycrystalline bulk LCO and in near-stoichiometric LCO single crystals, differentiating between *ab*-plane and *c*-axis, and compared both cases. For all cases, the same diffusion determination methodology was applied. We utilized lithium isotope heterostructures with ^{6}Li as a tracer and consecutive isotope depth profiling by SIMS. In this way, we can compare bulk diffusion of lithium in a polycrystal, that includes grain boundary diffusion, with lithium diffusion in the single crystal in *ab*-plane and along the *c*-axis as described in Section 1.3. Activation energies for lithium-ion migration were derived from the performed experiments using the Arrhenius law and discussed regarding the theoretical calculations available in the literature.

2. MATERIALS AND METHODS

Commercial LCO powder with an average particle size of 5 μm was obtained from Alfa Aesar, USA. After high-energy ball milling of the powder (4 × 1 min, SPEX 8000M shaker mill), compacted cylindrical samples of 8 mm diameter were prepared by pressing at 100 MPa. The pellets were sintered at T = 800 °C in air for t = 24 h. The heating was done at 3 K/min and subsequent cooling at the same rate. In order to study the intrinsic diffusion in the LCO compound, no binders, surface coatings, etc. commonly used for cathode material for batteries were added. The sintered LCO samples were analyzed by inductively coupled plasma-optical emission spectroscopy (ICP-OES) using a Plasma Quant 9100 (Analytik Jena) to determine the relative element concentrations. The structural investigation of the bulk LCO samples was performed by high-resolution X-ray diffraction (HRXRD) measurements in $\theta/2\theta$ mode after sintering, using a Bruker D8 DISCOVER diffractometer (Cu K_α, 40 keV, 40 mA). The microstructure of the sintered pellets was examined using high-resolution scanning electron microscopy (EVO 15, Zeiss). The average particle size and sample density were estimated from scanning electron microscopy (SEM) micrographs using the PxFworkbench software.

Commercial LCO single crystals grown by the flux method were obtained from OXIDE Corp, Japan. The samples had an average diameter of 10 mm, a thickness of ≈50 μm, and were cut into smaller pieces for the diffusion experiments. The crystals were (0001) oriented. The relative element concentrations were also analyzed by ICP-OES, and structural investigation was done by a $2\theta - \omega$ HRXRD scan after annealing at T = 800 °C in air for t = 1 h. The sample surface was investigated after annealing using SEM.

Tracer deposition was carried out by placing a thin layer of ^{6}Li isotope-enriched $^6LiCoO_2$ (6-LCO) with a thickness of ≈100 nm on the respective sample surface by ion beam sputtering, as shown in Figure 1. Ion-beam sputtering was carried out using a commercial setup (IBC 681, Gatan) equipped with two penning ion sources. The deposition was done at 5 keV and at 200 μA using argon sputter gas at an operation pressure of 5 × 10^{-3} mbar. In order to measure the lithium-ion diffusion in the *ab*-plane of the LCO single-crystal foils, the 6-LCO tracer was sputtered on the edge of the cut samples. The corresponding ^{6}Li-enriched sputter target was prepared by solid state syntheses using a two-step reaction route. $^6Li_2CO_3$ (95 at. % ^{6}Li) and Co_3O_4 powder were obtained commercially (Sigma-Aldrich, USA, and Carl Roth, Germany). The starting materials were mixed in a stoichiometric ratio in an agate ball-milling tank (Wisd WiseMix Ball Mill) at 150 rpm for t = 1 h with an appropriate amount of dispersing agent (ethanol). The black slurry was completely dried and then heated in pure oxygen for t = 24 h at T = 800 °C. After subsequent high-energy ball milling (SPEX 8000M shaker mill), a 2 cm diameter pellet was pressed at 330 MPa and sintered at T = 800 °C in air for t = 12 h, yielding a polycrystalline dense sputter target. For the diffusion experiments, the polycrystalline and monocrystalline LCO samples with sputtered 6-LCO tracer layer on top were annealed in air at the respective temperatures using a commercial rapid thermal annealing (RTA) setup (AO 600, MBE) as well as in an IR radiation-heated furnace (Quad Elliptical, RI Controls/Research Incorporated) which allows fast heating rates up to 100 K/s to ensure defined diffusion times.

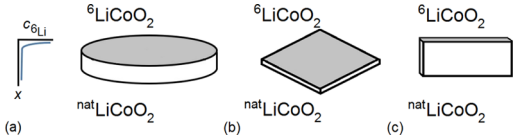

Figure 1. Illustration of the experimental method of ^{6}Li isotope tracer deposition on (a) sintered LCO pellets, (b) LCO single-crystal *c*-axis and (c) LCO single-crystal *ab*-plane. The tracer layer is shown in gray. The deposition of the ^{6}Li tracer leads to a lithium isotope gradient across the interface and therefore to the characteristic relative ^{6}Li fraction depth profile, as it is indicated in (a). For more details, see text.

The depth profiles of the lithium isotopes were measured by SIMS using a Cameca ims 3f/4f machine with O^- primary ions. SIMS is a complex depth or surface analysis technique for the chemical composition of a sample. In the depth profile mode, a beam of O^- primary ions is directed at the sample and scanned across the surface over an area of 250 × 250 μm. In the case of LCO single-crystal *ab*-plane investigations, the raster was reduced to 50 × 50 μm, and the samples were embedded into an aluminum oxide sample holder covered with silver paint to prevent sample charging. Secondary ions are released from the sample by sputtering. Since these carry a charge, the m/q ratio of the emitted secondary ions can be determined by SIMS in the mass filter region of the instrument (double focused mass spectrometer). Most of them are in the +1 or −1 charge state, and the determined mass equals the m/q ratio. Without comparative measurements on standard samples of known composition, no conclusions can be drawn about the concentration of the respective species in the sample. Therefore, the measure of the count rate is kept and only a depth profile is given. The time axis is converted into depth by measuring the final sputter crater using a stylus profilometer (Alphastep 500, Tencor). However, a statement on the relative isotope concentration $c(i)$ of species i in the sample can be derived because the ionization probabilities of isotopes are the same. The relative fraction of ^{6}Li is given by

$$c(^6\mathrm{Li}) = I(^6\mathrm{Li})/I(^6\mathrm{Li}) + I(^7\mathrm{Li}) \quad (1)$$

3. RESULTS

The results of the ICP-OES analysis of a sintered polycrystalline LCO sample as well as of a monocrystalline LCO sample under investigation are listed in Table 1 and indicate a near-stoichiometric composition for both types of materials. We get a lithium-to-metal ratio of x = 0.988 ± 0.014 (sintered polycrystalline sample) and x = 0.976 ± 0.014 (single crystal) close to the targeted ratio of x = 1.0. The element concentrations of both types of samples are identical within error limits.

The X-ray diffraction (XRD) patterns of a sintered polycrystalline LCO sample as well as a monocrystalline LCO sample are shown in Figure 2. All Bragg peaks

https://doi.org/10.1021/acs.chemmater.3c00359
Chem. Mater. 2023, 35, 3307−3315

Table 1. Relative Element Concentrations as Analyzed by ICP-OES of a Sintered Polycrystalline LCO Sample as Well as of a Monocrystalline LCO Sample under Investigation

	Li (at. %)	Co (at. %)	O (at. %)
LCO single crystal	23.68 ± 0.12	24.27 ± 0.21	52.05 ± 0.36
LCO polycrystalline sample	24.64 ± 0.13	24.94 ± 0.21	50.42 ± 0.34

correspond to the hexagonal α-$NaFeO_2$-type layered structure ($R\bar{3}m$ space group) without the appearance of any unknown diffraction peak. The lattice parameters are a = 2.815 Å and c = 14.060 Å and in good agreement to LCO.[11] The 003 peak has a full width at half-maximum of 0.12° resulting in crystallite sizes of about 70 nm calculated by the Scherrer formula. This indicates a nano-crystalline structure with a high density of grain boundaries. In Figure 2b, the $2\theta - \omega$ scan of a monocrystalline LCO sample is shown. Only three peaks can be detected, proving c-axis orientation in an out-of-plane direction. The absence of other peaks illustrates the high quality of the monocrystalline samples.

The LCO single-crystal surface and of the microstructure of the sintered LCO pellets were investigated by SEM. A SEM micrograph of a LCO cross section of a sintered pellet is shown in Figure 3a. As can be seen, secondary particles, that are much larger than the primary particle size of the as-received LCO powder, have grown during sintering. As the XRD measurements give a grain size of about 70 nm, we conclude that the secondary particles in Figure 3a are agglomerates of several grains. The relative density of the sintered LCO samples was estimated from SEM micrographs of a polished cross section (not shown) using the PxFworkbench software. A high relative density of 96.9 ± 1.6% and a low porosity were examined. A SEM micrograph of the surface of a monocrystalline LCO sample is shown in Figure 2b, which shows a smooth surface, without cracks or any other visible features.

Figure 4 shows characteristic SIMS depth profiles after tracer deposition and after diffusion annealing at T = 400 °C for a polycrystalline LCO sample in (a), a measurement along the LCO single-crystal c-axis in (b), and a measurement perpendicular to the c-axis in (c). The relative ^{6}Li fraction, c, is plotted as a function of sputter depth. The depth profile can be fitted using the thick film solution to Fick's second law pertaining to diffusion across an interface

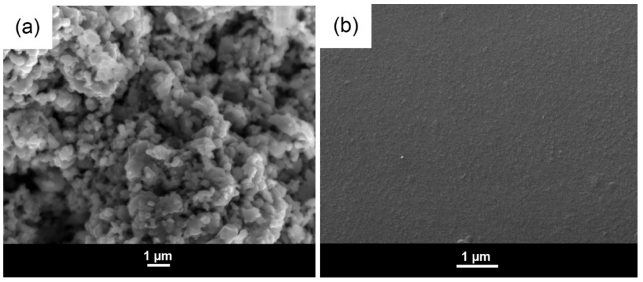

Figure 3. SEM micrographs of (a) freshly fractured cross section of a sintered LCO pellet (secondary electron image, 15 kV, 50,000 times magnification) and (b) surface of a monocrystalline LCO sample (secondary electron image, 20 kV, 100,000 times magnification) under investigation.

$$c(x,t) = c_\infty + \frac{(c_0 - c_\infty)}{2}\left[\mathrm{erf}\left(\frac{h+x}{R}\right) + \mathrm{erf}\left(\frac{h-x}{R}\right)\right] \quad (2)$$

with c_∞ being the residual ^{6}Li concentration in the LCO sample, c_0 being the ^{6}Li concentration present in the 6-LCO tracer layer, h being the thickness of the ^{6}Li-enriched layer, and R is the broadening of the lithium distribution at the interface. Annealing leads to diffusion of the ^{6}Li tracer into the sample connected with a broadening of the lithium distribution. For further analysis, the resulting ^{6}Li distributions in the diffusion annealed LCO samples were fitted by eq 2 in order to determine the lithium tracer diffusivities. In this context, c_∞, c_0 and R are free fit parameters, h is fixed to the initial value, and the fitting procedure was limited to data points which belong to the sample bulk, as can be seen in Figure 4.

The lithium tracer diffusivity D_{Li}* is determined from the difference in the respective broadening R of the lithium distribution of the diffusion profile and of the as-deposited profile, R_0, according to $D_{Li}^* = (R^2 - R_0^2)/4t$, where t is the annealing time interval. The results are displayed as a continuous red line in Figure 4. Slight deviations of the mathematical fit from the experimental data for $c < 0.15$, as can be seen in Figure 4b, are due to ion-beam mixing and interface roughness effects. They have no influence on the correct determination of the diffusivities. Diffusion annealings were carried out in the temperature range between 200 and 700 °C. An overview of the experimentally determined tracer diffusivities can be found in Table 2.

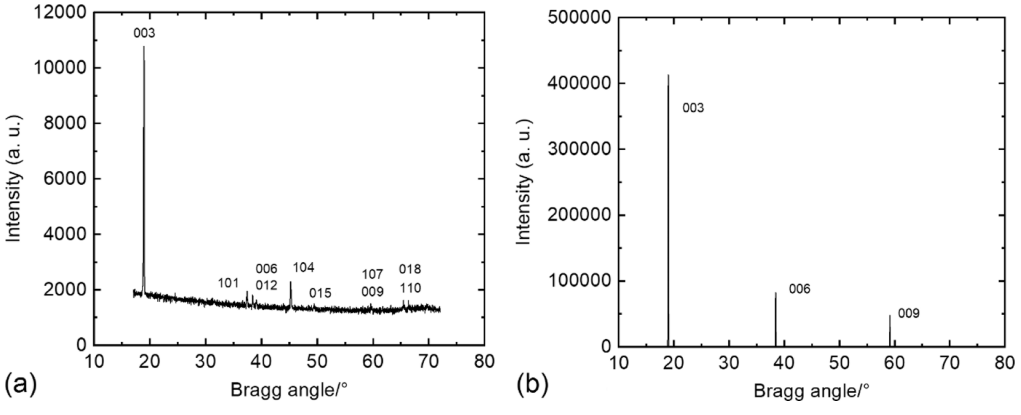

Figure 2. XRD patterns of (a) sintered polycrystalline LCO and (b) monocrystalline LCO sample under investigation.

https://doi.org/10.1021/acs.chemmater.3c00359
Chem. Mater. 2023, 35, 3307−3315

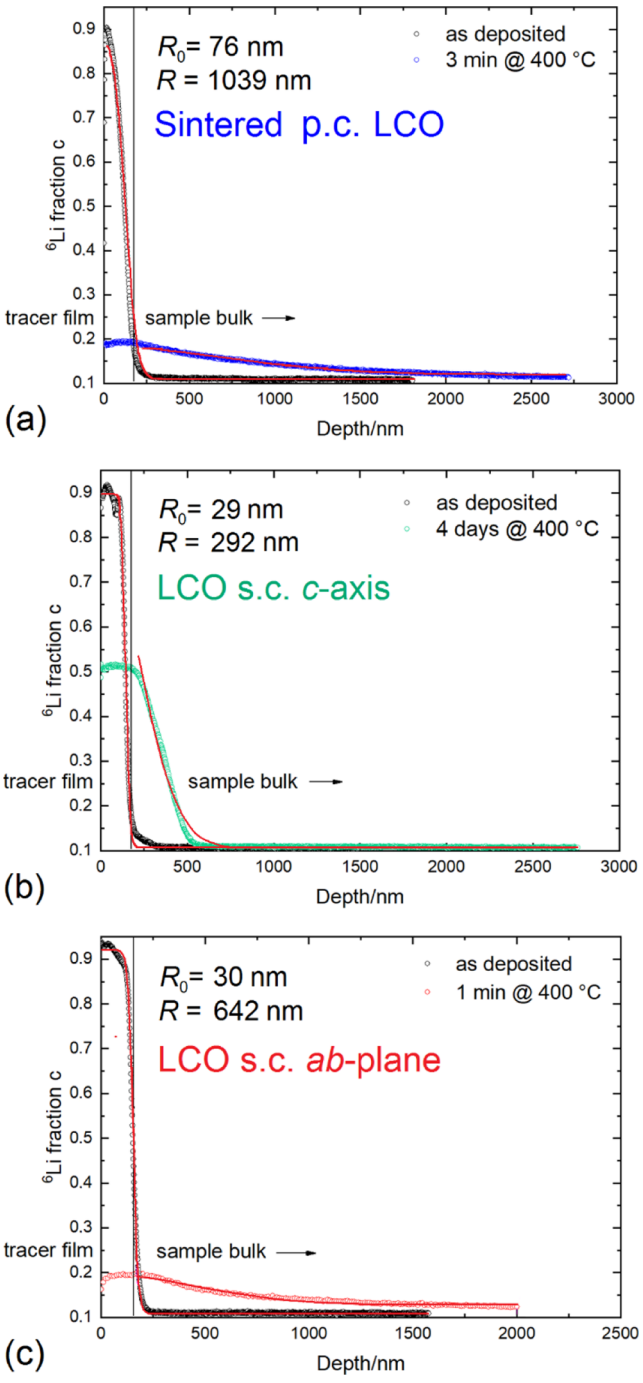

Figure 4. Relative ^{6}Li fraction after tracer deposition and after diffusion annealing at T = 400 °C for a sintered polycrystalline (p.c.) LCO sample in (a), a measurement along the LCO single crystal (s.c.) *c*-axis in (b), and a measurement along the LCO single-crystal *ab*-plane in (c).

In Figure 5 the determined tracer diffusivities are plotted as a function of the reciprocal temperature. The error limits of about 40% attributed to each diffusivity result in sum from the uncertainty in crater depth determination, from fitting, and from measuring at different locations on the sample surface with locally slightly differing diffusion behavior. The diffusivities obey the Arrhenius law

$$D_{Li}^{*} = D_0 \exp(\Delta H/k_B T) \quad (3)$$

Table 2. Lithium Tracer Diffusivities D_{Li}*, Annealing Times t, and Temperatures T of the Sintered Polycrystalline LCO Samples, the LCO Single-Crystal *c*-Axis, and the LCO Single-Crystal *ab*-Plane as Measured in This Study

sample	T/°C	t/min	D_{Li}*/m^2 s^{-1}
LCO sintered polycrystalline sample	200	1440	$(7.3 \pm 2.9) \times 10^{-18}$
	200	360	$(4.3 \pm 1.7) \times 10^{-18}$
	250	120	$(9.8 \pm 3.9) \times 10^{-17}$
	300	5	$(1.3 \pm 0.5) \times 10^{-16}$
	340	5	$(5.0 \pm 2) \times 10^{-16}$
	400	3	$(1.5 \pm 0.6) \times 10^{-15}$
	490	1	$(9.3 \pm 3.7) \times 10^{-15}$
LCO single crystal *c*-axis	400	6120	$(6.0 \pm 2.4) \times 10^{-20}$
	500	1440	$(3.5 \pm 1.4) \times 10^{-19}$
	600	60	$(2.5 \pm 1) \times 10^{-18}$
	700	20	$(1.0 \pm 0.4) \times 10^{-17}$
LCO single crystal *ab*-plane	200	3600	$(5.3 \pm 2.1) \times 10^{-18}$
	300	5	$(1.6 \pm 0.6) \times 10^{-16}$
	400	1	$(1.7 \pm 0.7) \times 10^{-15}$

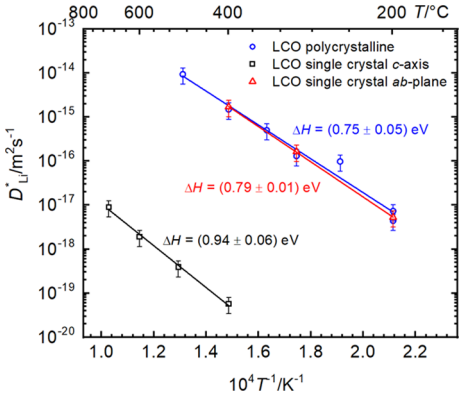

Figure 5. Lithium tracer diffusivities as a function of the reciprocal temperature as obtained by SIMS. Blue data points are for polycrystalline sintered LCO, black data points belong to monocrystalline LCO with measurements along the *c*-axis, and red data points belong to the same sample type but to measurements along the *ab*-plane. The solid lines represent least-squares fits of eq 3 to the diffusivities, which yield the respective activation enthalpies.

where ΔH is the activation enthalpy of diffusion, and D_0 is the pre-exponential factor. A least-squares fit of eq 3 to the diffusivities results in the respective activation enthalpies of ΔH = (0.75 ± 0.05) eV and a pre-exponential factor of D_0 = 7.9×10^{-10} m^2 s^{-1} (error: $\ln(D_0/\text{m}^2\ \text{s}^{-1}) = -20.96 \pm 1.40$) for the polycrystalline sintered LCO (blue symbols), ΔH = (0.94 ± 0.06) eV and a pre-exponential factor of $D_0 = 5.8 \times 10^{-13}$ m^2 s^{-1} (error: $\ln(D_0/\text{m}^2\ \text{s}^{-1}) = -28.17 \pm 1.65$) for the monocrystalline LCO *c*-axis (black symbols), and ΔH = (0.79 ± 0.01) eV and a pre-exponential factor of $D_0 = 1.4 \times 10^{-9}$ m^2 s^{-1} (error: $\ln(D_0/\text{m}^2\ \text{s}^{-1}) = -20.39 \pm 1.36$) for the monocrystalline LCO *ab*-plane (red symbols).

4. DISCUSSION

To discuss the lithium tracer diffusion in the polycrystalline LCO samples, two different enthalpies must be considered that can contribute to the total activation enthalpy of diffusion, ΔH, with $\Delta H = \Delta H_f + \Delta H_m$, where ΔH_f is the enthalpy of formation of the respective defect (lithium vacancy or interstitial) and ΔH_m is the enthalpy of lithium migration via

https://doi.org/10.1021/acs.chemmater.3c00359
Chem. Mater. 2023, 35, 3307−3315

a particular defect. The experimental data given in this work can be fitted with a single Arrhenius straight line, which suggests that a single mechanism is dominant over the temperature range (200 °C ≤ T ≤ 490 °C) investigated. The samples under investigation show a minor lithium deficit of about 1% (with respect to the error margin of the ICP-OES measurements), placing the sample composition at the lithium-poor side of the stability range.[15] The possible deviation from exact stoichiometry can be realized by pre-existing, athermal structural vacancies on the lithium sub-lattice (V_{Li}) in the single percent range. Therefore, thermally activated lithium vacancies (e.g., Schottky defects) can be neglected. That means that the experimentally determined activation enthalpy of diffusion is identical to the migration enthalpy of the lithium ions in the bulk: $\Delta H = \Delta H_m = 0.75$ eV (for a more thorough discussion, the reader is referred to ref 37).

Lithium-ion migration is believed to occur via a monovacancy mechanism (direct next neighbor hop of a lithium ion to a lithium vacancy V_{Li}^{-}), or a divacancy mechanism (DV_{Li}^{2-}), which involves a lithium divacancy (a pair of $V_{Li}-$).[12] The monovacancy mechanism occurs when the lithium deficit is small, while the divacancy mechanism is expected when the fraction of lithium vacancies is high, e.g., in the (partly) delithiated LCO cathode material. Hoang and Johannes[12] calculated values of 0.7 and 0.18 eV for the migration enthalpy of lithium ions in LCO for the monovacancy and divacancy mechanism, respectively, by a hybrid Hartree−Fock/DFT approach. Van der Ven and Ceder[17] calculated the migration enthalpy of lithium ions in LCO by the first principles pseudopotential method within the local density approximation of DFT for a lithium vacancy fraction of 0.1. They reported comparable results for ΔH_m of about 0.8 eV for the monovacancy mechanism and about 0.25 eV for the divacancy mechanism. A comparison of the calculated enthalpies to our experimental data shows that in the near-stoichiometric polycrystalline LCO the monovacancy mechanism is very likely the actual diffusion mechanism.

The model of structural lithium vacancies can be used to examine the pre-exponential factor, which is given by

$$D_0 = f_v a^2 \nu_0 \exp(\Delta S_m / k_B) \quad (4)$$

neglecting geometry and correlation factors. Here, $a = 2.86$ Å is the shortest lithium−lithium atomic distance, $\nu_0 \approx 1 \times 10^{13}$ s^{-1} is a characteristic vibration frequency, f_v is the fraction of structural lithium vacancies, and $\Delta S_m \approx 0\ k_B$ is the migration part of the entropy of diffusion. Using the experimentally determined pre-exponential factor $D_0 = 7.9 \times 10^{-10}$ m^2 s^{-1}, eq 4 can be used to calculate the fraction of structural lithium vacancies to $f_v \approx 0.001$. This agrees to the results of the ICP-OES measurements within error limits.

Next, we discuss the results on the single crystal. As mentioned in Section 1.3, the perfect LCO crystal is composed of CoO_2 layers stacked in the [0001] direction with lithium intercalated in between, which forms a 2d network parallel to the (0001) plane.[26] Due to its layered structure, LCO is a 2d lithium-ion conductor, where, in the perfect crystal, diffusion along the c-axis is expected to be unlikely to occur, which is due to a calculated very high energy barrier of 6.8 eV for direct penetration of the CoO_2 layers.[26−28] First, lithium-ion diffusion in the ab-plane, perpendicular to the c-axis, is discussed. The diffusivities are given as red symbols in Figure 5. The results show that at T = 200, 300, and 400 °C, the lithium tracer diffusivities are identical, within error limits, to the diffusivities measured in the polycrystalline LCO samples (blue symbols in Figure 5). We determine an activation enthalpy of $\Delta H = 0.79$ eV, which is identical, within error limits, to the one determined for lithium-ion migration in the polycrystalline LCO, as well. This is very astonishing and gives rise to two important consequences. First, we can conclude that in polycrystalline LCO the bulk diffusion of lithium ions occurs preferably via the ab-plane (Figure 5) and second, that the lithium-ion diffusivities in LCO grain boundaries (D_{gb}) and in the bulk ab-plane (D_b) have to be very similar. Otherwise, the identical results on lithium-ion diffusion in polycrystalline and monocrystalline samples cannot be understood. The reason for this observation is the nature of the underlying diffusion mechanism. As previously discussed, the measured activation enthalpy and the low fraction of structural lithium vacancies point to the monovacancy mechanism. The latter determines the lithium diffusion in the grain or in the bulk. An increased concentration of lithium vacancies in the grain boundaries, as discussed in the literature,[46] would in this case have little influence, as will be shown in the following section. In addition, the theoretically calculated migration energies for lithium migration via a monovacancy mechanism along a grain boundary are very similar to the activation energies in the bulk, as discussed in Section 1.3 (refs 26 and 28) and therefore do not give any decisive, experimentally measurable advantage for lithium-ion diffusion. That means that the long-range diffusion of lithium takes place in a Harrison type A diffusion kinetics regime,[47,48] which is defined as $(D_b\, t)^{1/2} \geq d/0.8$,[43] with $d = 70$ nm being the diameter of the grains. This condition is fulfilled according to Table 2. In the Harrison type A regime, a distinction between bulk diffusion and grain boundary diffusion is not possible and effective diffusivities are measured. However, our results can only be explained if both diffusivities, in LCO bulk and grain boundaries, are similar. If lithium-ion diffusion in LCO grain boundaries would be significantly faster, higher effective diffusivities would also be expected according to $D_{eff} = gD_{gb} + (1 - g)\ D_b$, where $g \approx 3\delta/d \approx 0.04$ is the volume fraction of grain boundaries and $\delta \approx 1$ nm is the diameter of the grain boundary. Consequently, the difference between D_b and D_{gb} could be only in the range of one order of magnitude at maximum.

These important findings must be discussed regarding the application of LCO powder in LIB cathodes as well. Since LCO derivatives like NMC have the same characteristic layered crystal structure, in which the lithium ions diffuse, it can be assumed that our conclusions are valid for NMC-based cathode material as well.[40,49] It is common sense that the lithium-ion transport within the active material is the limiting process among different lithium-ion transport pathways in a battery cathode, where the electrode materials with the highest lithium diffusion coefficients are also the materials with the best rate performance.[49] General strategies for battery performance enhancement of electrode materials (anode and cathode) include (a) dimension reduction, (b) composite formation, (c) doping and functionalization, (d) morphology control, and (e) coating and encapsulation.[3] The idea behind strategy (a), which includes the introduction of so-called nanoparticles and nanostructures, is that the rate performance can be improved by shortening the lithium-ion diffusion length.[3] The avoidance of grain boundaries and the use of monocrystalline particles in the micrometer dimension (≈5 μm) seems to be a sensible contribution to the strategy (d).[50]

https://doi.org/10.1021/acs.chemmater.3c00359
Chem. Mater. 2023, 35, 3307−3315

Grain boundaries are detrimental to mechanical stability, as they are associated with micro-crack growth (especially, micron-sized secondary particles, which are aggregated by nanosized primary particles, as in this study, can crack, promoted by the strain at high-voltage operation) and also with potential barriers along the grains. As recently discussed by Klein et al.,[50] larger primary particles are supposed to be mechanically more stable with regard to intra-granular cracking and, even more important, the behavior of single-crystal-based cathode material under high-voltage conditions (4.4−4.7 V) shows significant performance enhancement due to appropriate morphological alteration. Since, contrary to the established view, this work shows that there is no advantage in the form of much faster lithium-ion diffusion in the grain boundaries, the strategy to avoid them has found new confirmation.

Finally, the experimental data on the *c*-axis lithium-ion diffusion in the LCO single crystals determined in this study have to be discussed. As seen in Figure 5, the diffusivities are lower by roughly five orders of magnitude. However, we determine an activation enthalpy of ΔH = 0.94 eV, which is far off the calculations of the energy barrier of 6.8 eV for direct penetration of the CoO_2 layers. The reduction in diffusivities for *c*-axis migration (compared to the *ab*-plane) is not only due to the slightly higher activation energy (0.94 eV instead of 0.79 eV) but also due to the reduced pre-exponential factor of $D_0 = 5.83 \times 10^{-13}$ m^2/s (compared to $D_0 = 1.4 \times 10^{-9}$ m^2/s^{-1}). We agree with the model proposed by Hasegawa et al.[27] for *c*-axis diffusion in LCO, which says that in the single crystal the lithium-ion diffusion along the *c*-axis is determined by diffusion in the *ab*-plane, and the transfer across the CoO_2 layers occurs via rare defects with a low migration energy barrier. In the case of lithium antisites and oxygen vacancies, a migration enthalpy of 1 eV was calculated by DFT.[27] Due to the small number of defects (low pre-exponential factor), the probability for penetration is low. As a result, we get experimentally for the single-crystal *c*-axis diffusion an activation enthalpy of 0.94 eV, which is close to the calculated value of 1 eV, but very low lithium-ion diffusivities, with a low pre-exponential factor, when compared to the lithium-ion diffusivities determined in polycrystalline LCO.

5. CONCLUSIONS

We carried out lithium tracer diffusion studies by means of ^6Li isotope exchange and consecutive SIMS measurements in the temperature range of 200−700 °C. Lithium-ion diffusivities in near-stoichiometric sintered polycrystalline bulk LCO with an average grain size of about 70 nm and near-stoichiometric LCO single crystals (*ab*-plane and *c*-axis) were compared for the first time. The lithium-ion diffusivity along the *c*-axis was measured to be orders of magnitude (e.g., at T = 400 °C, five orders of magnitude) lower than the one measured perpendicular to the *c*-axis, confirming theoretically predicted indications. The results of the diffusion experiments revealed that, for polycrystalline LCO, the monovacancy mechanism via structural lithium vacancies is very likely the diffusion mechanism in the temperature range investigated. The activation enthalpy was determined to $\Delta H = \Delta H_m$ = 0.75 eV, in good agreement to theoretical calculations. Considering the *c*-axis lithium-ion diffusion in the LCO single crystals, we determined an activation enthalpy of ΔH = 0.94 eV, which is far off the energy barrier of 6.8 eV which was calculated for the direct penetration of the CoO_2 layers by lithium ions. Compared to the results determined in the polycrystalline LCO, the lithium diffusivities were nevertheless lower by some orders of magnitude. The lithium-ion diffusion along the *c*-axis is most likely determined by diffusion in the *ab*-plane, and the transfer across the CoO_2 layers occurs via rare defects, with lithium antisites and oxygen vacancies, as suggested in the literature. In contrast to this, our results on the *ab*-plane lithium-ion diffusion in the LCO single crystals show that the diffusivities are very similar compared to the ones determined in the sintered polycrystalline LCO samples. We conclude that in polycrystalline LCO, the lithium-ion diffusion in grain boundaries and in the bulk *ab*-plane is similar and that grain boundaries do not play a dominating role in lithium-ion migration.

AUTHOR INFORMATION

Corresponding Author

Daniel Uxa − *Institute of Metallurgy, Solid State Kinetics Group, Clausthal University of Technology, Clausthal-Zellerfeld 38678, Germany;* orcid.org/0000-0002-4583-619X; Email: daniel.uxa@tu-clausthal.de

Authors

Erwin Hüger − *Institute of Metallurgy, Solid State Kinetics Group, Clausthal University of Technology, Clausthal-Zellerfeld 38678, Germany; Clausthal Centre of Material Technology, Clausthal-Zellerfeld 38678, Germany;* orcid.org/0000-0002-1545-1459

Kevin Meyer − *Institute of Energy Research and Physical Technologies, Energy Conversion Group, Clausthal University of Technology, Clausthal-Zellerfeld 38678, Germany*

Lars Dörrer − *Institute of Metallurgy, Solid State Kinetics Group, Clausthal University of Technology, Clausthal-Zellerfeld 38678, Germany*

Harald Schmidt − *Institute of Metallurgy, Solid State Kinetics Group, Clausthal University of Technology, Clausthal-Zellerfeld 38678, Germany; Clausthal Centre of Material Technology, Clausthal-Zellerfeld 38678, Germany;* orcid.org/0000-0001-9389-8507

Complete contact information is available at: https://pubs.acs.org/10.1021/acs.chemmater.3c00359

Notes

The authors declare no competing financial interest.

ACKNOWLEDGMENTS

This work was funded by the Deutsche Forschungsgemeinschaft (DFG, German Research Foundation) [SCHM 1569/33; INST 189/194 FUGG]. The financial support is gratefully acknowledged. We are indebted to G. Zander for ICP-OES analysis and helpful discussions, to H. J. Holmes for preparing the sintered LCO samples, and to S. Lenk for SEM measurements.

REFERENCES

(1) Li, M.; Lu, J.; Chen, Z.; Amine, K. 30 Years of Lithium-Ion Batteries. *Adv. Mater.* **2018**, *30*, 1800561−1800585.

(2) Etacheri, V.; Marom, R.; Elazari, R.; Salitra, G.; Aurbach, D. Challenges in the development of advanced Li-ion batteries: a review. *Energy Environ. Sci.* **2011**, *4*, 3243−3262.

(3) Nitta, N.; Wu, F.; Lee, J. T.; Yushin, G. Li-ion battery materials: present and future. *Mater. Today* **2015**, *18*, 252−264.

(4) Manthiram, A. A reflection on lithium-ion battery cathode chemistry. *Nat. Commun.* **2020**, *11*, 1550.
(5) Blomgren, G. E. The Development and Future of Lithium Ion Batteries. *J. Electrochem. Soc.* **2016**, *164*, A5019−A5025.
(6) Chen, R.; Zhao, T.; Zhang, X.; Li, L.; Wu, F. Advanced cathode materials for lithium-ion batteries using nanoarchitectonics. *Nanoscale Horiz.* **2016**, *1*, 423−444.
(7) Xu, J.; Dou, S.; Liu, H.; Dai, L. Cathode materials for next generation lithium ion batteries. *Nano Energy* **2013**, *2*, 439−442.
(8) Julien, C.; Mauger, A.; Vijh, A. *Lithium Batteries: Science and Technology*; Springer International Publishing, 2016.
(9) Liu, C.; Neale, Z. G.; Cao, G. Understanding electrochemical potentials of cathode materials in rechargeable batteries. *Mater. Today* **2016**, *19*, 109−123.
(10) Julien, C.; Mauger, A.; Zaghib, K.; Groult, H. Optimization of Layered Cathode Materials for Lithium-Ion Batteries. *Materials* **2016**, *9*, 595.
(11) Reimers, J. N.; Dahn, J. R. Electrochemical and In Situ X-Ray Diffraction Studies of Lithium Intercalation in Li_xCoO_2. *J. Electrochem. Soc.* **1992**, *139*, 2091−2097.
(12) Hoang, K.; Johannes, M. D. Defect physics in complex energy materials. *J. Phys.: Condens. Matter* **2018**, *30*, 293001−293022.
(13) Hoang, K.; Johannes, M. D. Tailoring Native Defects in $LiFePO_4$: Insights from First-Principles Calculations. *Chem. Mater.* **2011**, *23*, 3003−3013.
(14) Hoang, K.; Johannes, M. D. First-principles studies of the effects of impurities on the ionic and electronic conduction in $LiFePO_4$. *J. Power Sources* **2012**, *206*, 274−281.
(15) Hoang, K.; Johannes, M. D. Defect chemistry in layered transition-metal oxides from screened hybrid density functional calculations. *J. Mater. Chem. A* **2014**, *2*, 5224−5235.
(16) Hoang, K.; Johannes, M. D. Defect Physics and Chemistry in Layered Mixed Transition Metal Oxide Cathode Materials: (Ni,Co,Mn) vs (Ni,Co,Al). *Chem. Mater.* **2016**, *28*, 1325−1334.
(17) Van der Ven, A.; Ceder, G. Lithium Diffusion in Layered Li_xCoO_2. *Electrochem. Solid-State Lett.* **2000**, *3*, 301−304.
(18) Van der Ven, A.; Ceder, G. Lithium diffusion mechanisms in layered intercalation compounds. *J. Power Sources* **2001**, *97*−*98*, 529−531.
(19) Ceder, G.; Doyle, M.; Arora, P.; Fuentes, Y. Computational Modeling and Simulation for Rechargeable Batteries. *MRS Bull.* **2002**, *27*, 619−623.
(20) Bhatt, M. D.; O'Dwyer, C. Recent progress in theoretical and computational investigations of Li-ion battery materials and electrolytes. *Phys. Chem. Chem. Phys.* **2015**, *17*, 4799−4844.
(21) Fallahzadeh, R.; Farhadian, N. Molecular dynamics simulation of lithium ion diffusion in LiCoO2 cathode material. *Solid State Ionics* **2015**, *280*, 10−17.
(22) Islam, M. S.; Fisher, C. A. J. Lithium and sodium battery cathode materials: computational insights into voltage, diffusion and nanostructural properties. *Chem. Soc. Rev.* **2014**, *43*, 185−204.
(23) Urban, A.; Seo, D.-H.; Ceder, G. Computational understanding of Li-ion batteries. *npj Comput. Mater.* **2016**, *2*, 16002.
(24) van der Ven, A.; Bhattacharya, J.; Belak, A. A. Understanding Li diffusion in Li-intercalation compounds. *Acc. Chem. Res.* **2013**, *46*, 1216−1225.
(25) Heitjans, P. Lithium Ions in solids − Between Basics and Better Batteries. *Z. Phys. Chem.* **2015**, *229*, 1263−1264.
(26) Zhu, X.; Ong, C. S.; Xu, X.; Hu, B.; Shang, J.; Yang, H.; Katlakunta, S.; Liu, Y.; Chen, X.; Pan, L.; Ding, J.; et al. Direct observation of lithium-ion transport under an electrical field in Li_xCoO_2 nanograins. *Sci. Rep.* **2013**, *3*, 1084.
(27) Hasegawa, G.; Kuwata, N.; Tanaka, Y.; Miyazaki, T.; Ishigaki, N.; Takada, K.; Kawamura, J. Tracer diffusion coefficients of Li^+ ions in *c*-axis oriented Li_xCoO_2 thin films measured by secondary ion mass spectrometry. *Phys. Chem. Chem. Phys.* **2021**, *23*, 2438−2448.
(28) Moriwake, H.; Kuwabara, A.; Fisher, C. A. J.; Huang, R.; Hitosugi, T.; Ikuhara, Y. H.; Oki, H.; Ikuhara, Y. First-Principles Calculations of Lithium-Ion Migration at a Coherent Grain Boundary in a Cathode Material, $LiCoO_2$. *Adv. Mater.* **2013**, *25*, 618−622.
(29) Xia, H.; Lu, L.; Ceder, G. Li diffusion in $LiCoO_2$ thin films prepared by pulsed laser deposition. *J. Power Sources* **2006**, *159*, 1422−1427.
(30) Shiraki, S.; Oki, H.; Hitosugi, T. Li diffusion in (110)-oriented $LiCoO_2$ thin films grown on Au and Pt (110) substrates. *Surf. Interface Anal.* **2016**, *48*, 1240−1243.
(31) Stolz, L.; Gaberšček, M.; Winter, M.; Kasnatscheew, J. Different Efforts but Similar Insights in Battery R&D: Electrochemical Impedance Spectroscopy vs Galvanostatic (Constant Current) Technique. *Chem. Mater.* **2022**, *34*, 10272−10278.
(32) Vinod Chandran, C.; Heitjans, P. Solid-State NMR Studies of Lithium Ion Dynamics Across Materials Classes. *Annual Reports on NMR Spectroscopy*; Annual Reports on NMR Spectroscopy; Webb, G. A., Ed.; Elsevier, 2016; Vol. *89*, pp 1−102.
(33) Tomeno, I.; Oguchi, M. NMR Study of $LiCo_{1-x}Cr_xO_2$ and $Li_{1-x}Na_xCoO_2$ (x = 0 and 0.05). *J. Phys. Soc. Jpn.* **1998**, *67*, 318−322.
(34) Nakamura, K.; Yamamoto, M.; Okamura, K.; Michihiro, Y.; Nakabayashi, I.; Kanashiro, T. NMR investigation on the motion of Li^+ defects in $LiCoO_2$ and $LiNiO_2$. *Solid State Ionics* **1999**, *121*, 301−306.
(35) Nakamura, K.; Ohno, H.; Okamura, K.; Michihiro, Y.; Moriga, T.; Nakabayashi, I.; Kanashiro, T. ^7Li NMR study on Li^+ ionic diffusion and phase transition in Li_xCoO_2. *Solid State Ionics* **2006**, *177*, 821−826.
(36) Nakamura, K.; Hirano, H.; Nishioka, D.; Michihiro, Y.; Moriga, T. Lithium ionic diffusion in lithium cobalt oxides prepared by mechanical milling. *Solid State Ionics* **2008**, *179*, 1806−1809.
(37) Mehrer, H. *Diffusion in Solids: Fundamentals, Methods, Materials, Diffusion-Controlled Processes*; Springer Berlin Heidelberg, 2007.
(38) Rahn, J.; Hüger, E.; Dörrer, L.; Ruprecht, B.; Heitjans, P.; Schmidt, H. Li self-diffusion in lithium niobate single crystals at low temperatures. *Phys. Chem. Chem. Phys.* **2012**, *14*, 2427.
(39) Uxa, D.; Holmes, H. J.; Meyer, K.; Dörrer, L.; Schmidt, H. Lithium Tracer Diffusion in Sub-Stoichiometric Layered Lithium-Metal-Oxide Compounds. *Defect Diffus. Forum* **2021**, *413*, 125−135.
(40) Uxa, D.; Holmes, H. J.; Meyer, K.; Dörrer, L.; Schmidt, H. Lithium tracer diffusion in $LiNi_{0.33}Mn_{0.33}Co_{0.33}O_2$ cathode material for lithium-ion batteries. *Phys. Chem. Chem. Phys.* **2021**, *23*, 5992−5998.
(41) Uxa, D.; Schmidt, H. Lithium Tracer Diffusion in Near Stoichiometric $LiNi_{0.5}Mn_{1.5}O_4$ Cathode Material for Lithium-Ion Batteries. *Z. Phys. Chem.* **2022**, *236*, 979−989.
(42) Kuwata, N.; Nakane, M.; Miyazaki, T.; Mitsuishi, K.; Kawamura, J. Lithium diffusion coefficient in $LiMn_2O_4$ thin films measured by secondary ion mass spectrometry with ion-exchange method. *Solid State Ionics* **2018**, *320*, 266−271.
(43) Kuwata, N.; Hasegawa, G.; Maeda, D.; Ishigaki, N.; Miyazaki, T.; Kawamura, J. Tracer Diffusion Coefficients of Li Ions in $Li_xMn_2O_4$ Thin Films Observed by Isotope Exchange Secondary Ion Mass Spectrometry. *J. Phys. Chem. C* **2020**, *124*, 22981−22992.
(44) Schwab, C.; Höweling, A.; Windmüller, A.; Gonzalez-Julian, J.; Möller, S.; Binder, J. R.; Uhlenbruck, S.; Guillon, O.; Martin, M. Bulk and grain boundary Li-diffusion in dense $LiMn_2O_4$ pellets by means of isotope exchange and ToF-SIMS analysis. *Phys. Chem. Chem. Phys.* **2019**, *21*, 26066−26076.
(45) Takai, S.; Yoshioka, K.; Iikura, H.; Matsubayashi, M.; Yao, T.; Esaka, T. Tracer diffusion coefficients of lithium ion in $LiMn_2O_4$ measured by neutron radiography. *Solid State Ionics* **2014**, *256*, 93−96.
(46) Parras, J. P.; De Souza, R. A. Grain-boundary diffusion of cations in fluorite-type oxides is faster but not always easier. *Acta Mater.* **2020**, *195*, 383−391.
(47) Harrison, L. G. Influence of dislocations on diffusion kinetics in solids with particular reference to the alkali halides. *Trans. Faraday Soc.* **1961**, *57*, 1191.

https://doi.org/10.1021/acs.chemmater.3c00359
Chem. Mater. 2023, 35, 3307−3315

(48) Belova, I. V.; Murch, G. E. The transition from Harrison type-B to type-A kinetics in grain-boundary tracer diffusion. *Philos. Mag. A* **2001**, *81*, 2447−2455.
(49) Kasnatscheew, J.; Rodehorst, U.; Streipert, B.; Wiemers-Meyer, S.; Jakelski, R.; Wagner, R.; Laskovic, I. C.; winter, M. Learning from Overpotentials in Lithium Ion Batteries: A Case Study on the $LiNi_{1/3}Co_{1/3}Mn_{1/3}O_2$ (NCM) Cathode. *J. Electrochem. Soc.* **2016**, *163*, A2943−A2950.
(50) Klein, S.; Bärmann, P.; Fromm, O.; Borzutzki, K.; Reiter, J.; Fan, Q.; Winter, M.; Placke, T.; Kasnatscheew, J. Prospects and limitations of single-crystal cathode materials to overcome cross-talk phenomena in high-voltage lithium ion cells. *J. Mater. Chem. A* **2021**, *9*, 7546−7555.

https://doi.org/10.1021/acs.chemmater.3c00359
Chem. Mater. 2023, 35, 3307−3315